Nanoscale

PAPER

View Article Online
View Journal | View Issue

Cite this: *Nanoscale*, 2016, **8**, 17854

Nonlinear Rashba spin splitting in transition metal dichalcogenide monolayers†

Cai Cheng,[a,b] Jia-Tao Sun,*[a] Xiang-Rong Chen,*[b] Hui-Xia Fu[a] and Sheng Meng*[a,c]

Received 25th May 2016,
Accepted 13th September 2016

DOI: 10.1039/c6nr04235j

www.rsc.org/nanoscale

Single-layer transition-metal dichalcogenides (TMDs) such as MoS_2 and $MoSe_2$ exhibit unique electronic band structures ideal for hosting many exotic spin-orbital orderings. It has been widely accepted that Rashba spin splitting (RSS) is linearly proportional to the external field in heterostructure interfaces or to the potential gradient in polar materials. Surprisingly, an extraordinary nonlinear dependence of RSS is found in semiconducting TMD monolayers under a gate field. In contrast to small and constant RSS in polar materials, the potential gradient in non-polar TMDs gradually increases with the gate bias, resulting in nonlinear RSS with a Rashba coefficient an order-of-magnitude larger than the linear one. Most strikingly, under a large gate field $MoSe_2$ demonstrates the largest anisotropic spin splitting among all known semiconductors to our knowledge. Based on the $\boldsymbol{k}\cdot\boldsymbol{p}$ model *via* symmetry analysis, we identify that the third-order contributions are responsible for the large nonlinear Rashba splitting. The gate tunable spin splitting found in semiconducting pristine TMD monolayers promises future spintronics applications in that spin polarized electrons can be generated by external gating in an experimentally accessible way.

1. Introduction

Two-dimensional (2D) transition-metal dichalcogenides (TMDs) (Fig. 1a) have attracted intensive attention thanks to their potential in various applications such as nanoscale electronics, photonics, valleytronics, and spintronics.[1–9] On the other hand, the search for materials with strong spin–orbit coupling (SOC) has been one of the central themes in the materials science community. A significant discovery is the Rashba effect,[10–12] which relies on the spin–orbit coupling (SOC) of the carriers, thus in a two-dimensional electron gas a vertical electric field E is seen by a moving electron as a magnetic field that couples to its spin in the xy-plane. In other words, the spin degeneracy of electronic states can be lifted by the out-of-plane electric potential gradient, breaking the inversion symmetry. Rashba spin splitting (RSS) has been observed in metallic surfaces,[13–16] semiconductor heterostructures,[17,18] ultrathin metal films,[19,20] and topological insulators.[21–23] The effective Rashba Hamiltonian with the spin–orbit term has the isotropic form $H_{\mathrm{R}}^{\mathrm{iso}}(k) = \alpha_{\mathrm{R}}^{\mathrm{iso}}(k_x\sigma_y - k_y\sigma_x)$. Here σ_x and σ_y denote the Pauli matrices, and k is the two-dimensional quasimomentum. The energy spectrum consists of two branches in the form $E_{\pm}^{\mathrm{iso}}(k) = \dfrac{\hbar^2 k^2}{2m^*} \pm \alpha_{\mathrm{R}}^{\mathrm{iso}}|k|$. The relationship describes two

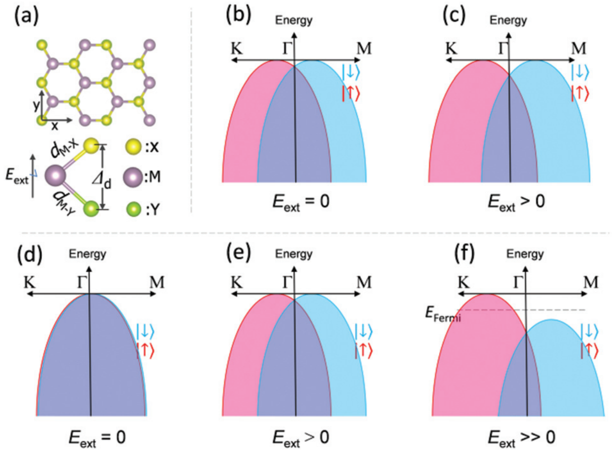

Fig. 1 Top and side view of the monolayer MX_2 and MXY (M = Mo, W; X/Y = S, Se) unit cell. (b), (c) Schematic view of RSS in polar systems (|↑⟩ and |↓⟩ stand for spin-up and spin-down states) with potential gradients in the vertical direction. Schematics of spin-degenerate bands (slightly shifted for clarity) (d), isotropic Rashba splitting under a small electric field (e) and anisotropic Rashba splitting with a large electric field (f) in the non-polar TMDs.

---

[a] *Beijing National Laboratory for Condensed Matter Physics and Institute of Physics, Chinese Academy of Sciences, Beijing 100190, China. E-mail: jtsun@iphy.ac.cn*
[b] *College of Physical Science and Technology, Sichuan University, Chengdu 610064, China. E-mail: xrchen@scu.edu.cn*
[c] *School of Physical Sciences, University of Chinese Academy of Sciences, Beijing 100190, China. E-mail: smeng@iphy.ac.cn*

† Electronic supplementary information (ESI) available: Atomic and electronic structures of monolayer TMDs; the planar averaged electrostatic potential and dipole moment; the comparison of Rashba splitting for monolayer $MoSe_2$ and MoS_2; the Rashba splitting and spin texture for $MoSe_2$; the Rashba splitting of MoSSe; the nonlinear Rashba splitting of $MoSe_2$; the Rashba splitting of $MoSe_2$ and WSe_2. See DOI: 10.1039/c6nr04235j

parabolas that shifted by $\pm\Delta k$ off the origin. For a surface the origin of the electric field E is the potential gradient perpendicular to the surface. This shows an isotropic splitting for $k \neq 0$, and at least for moderate values of k, they can be readily fit to experimentally and *ab initio* dispersion relations. Then the isotropic Rashba coefficient from the free electron model is obtained as $\alpha_{\mathrm{R}}^{\mathrm{iso}} = \frac{\hbar^2}{4m^2c^2}\int \mathrm{d}^3r|\phi(z)|^2\partial_z V(r)$.[24]

It is obvious that in addition to the atomic SOC, the out-of-plane field is assumed – but need not – to be necessary to have the Rashba effect. For example, the inherent electrostatic potential gradient in single-layer polar MoSSe (hereafter polar or non-polar denotes if there exists the intrinsic electrostatic potential gradient or not as shown in Fig. 1a) can lead to a zero-field isotropic Rashba splitting of $\alpha_{\mathrm{R}}^{\mathrm{iso}} = 0.067$ eV Å (Fig. 1b). The isotropic Rashba spin splitting can be tuned by means of an external electric gate with a linear scaling behavior with respect to field strength (Fig. 1c and S5†). If there is no electrostatic potential gradient, for example in non-polar 2H-$\mathrm{MoS_2}$ with an equivalent bond length $d_{\mathrm{M-X}} = d_{\mathrm{M-Y}}$ shown in Fig. 1a, the Rashba spin splitting could be neglected as commonly expected. Consequently, the controllable generation of Rashba spin splitting in TMD materials without an intrinsic vertical potential gradient is desirable for efficient spintronic devices.

Here we report that an extraordinary nonlinear Rashba effect can be generated in 2H-$\mathrm{MX_2}$ (M = Mo, W; X = S, Se). Although it is well known that the surface band structure undergoes Rashba spin splitting under a strong external field normal to the surface, a strong nonlinear dependence of the Rashba spin splitting with the external field is rarely reported, especially in atomically thin 2D materials. Hereafter $\mathrm{MX_2}$ denotes the 2H polytype monolayers by applying an external gate bias. The resulting effective Rashba coefficient is an order of magnitude larger than that of polar TMDs and regular semiconductor heterointerfaces made of elements of similar atomic masses, and is comparable to metallic surfaces made of heavy metals (Bi, Au *etc*). In contrast, polar MoSSe presents only a small Rashba spin splitting which is linear to the gate bias applied. The nonlinearity in RSS for symmetric TMDs is attributed to the large anisotropic momentum and energy splitting in the Brillouin zone. Most strikingly, $\mathrm{MoSe_2}$ demonstrates the largest anisotropy among all known semiconductors to our knowledge, in spin splitting along the Γ–K and Γ–M directions under a gate field larger than 0.5 V Å^{-1}. The largest anisotropy in RSS was explained by the effective $\boldsymbol{k}\cdot\boldsymbol{p}$ theory which includes high-order spin–orbit coupling. The anisotropic spin splitting predicted here and the semiconducting nature of the hosting 2D materials can be used to generate spin-polarized currents in gate-tunable TMD monolayers, promising for future spin injection and other nonmagnetic spintronics devices.

2. Methods

The geometry optimization and the electronic structure of the polar and non-polar TMD monolayers are obtained based on first-principles plane wave calculations within density functional theory as implemented in the Vienna *ab initio* simulation package (VASP).[25–27] The projector augmented-wave method[28] and the Perdew–Burke–Ernzerhof exchange–correlation functional[29] are used. A cutoff energy of 500 eV for the plane-wave basis set and a Monkhorst–Pack mesh[30] of 11 × 11 × 1 for the Brillouin zone integration are employed for relaxation and 21 × 21 × 1 for self-consistent calculations. In order to eliminate the interaction between two adjacent monolayers, a vacuum layer of thickness larger than 17 Å is adopted in the calculations in order to avoid spurious interactions due to the nonlocal nature of the correlation energy. All the structures are fully relaxed by a conjugate gradient method until the maximum Hellmann–Feynman force acting on each atom is less than 0.01 eV Å^{-1}. The electric gate field normal to the slab is realized by introducing a dipole sheet in the middle of the vacuum layer.[31] The phonon dispersion is calculated using the density functional perturbation theory.[32,33]

3. Results and discussion

3.1 Band structures, local potentials and energy differences for TMDs

Fig. 2a–c show the electronic band structure of $\mathrm{MoS_2}$ with SOC in the presence of a vertical electric field E_{ext} = 0.0 V Å^{-1}, 0.5 V Å^{-1} and 0.75 V Å^{-1}, respectively, where the first Brillouin zone

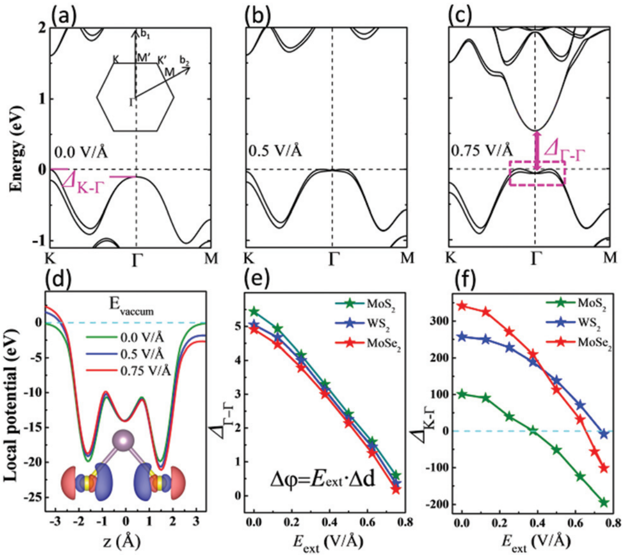

Fig. 2 (a–c) Electronic band structure of $\mathrm{MoS_2}$ with SOC at E_{ext} = 0.0, 0.5, and 0.75 V Å^{-1} respectively. The hexagon in the inset of (a) is the first Brillouin zone. (d) The planar averaged local potential of $\mathrm{MoS_2}$ with E_{ext} = 0.0 (olive line), 0.5 V Å^{-1} (blue line), and 0.75 V Å^{-1} (red line). The potentials are shifted with respect to the vacuum level (zero energy). The inset is the charge density difference between E_{ext} = 0.5 V Å^{-1} and 0 V Å^{-1}. Red (blue) color represents the electron accumulation (depletion) region. The isosurface value is set at 1.8 × 10^{-3} e Å^{-3}. (e), (f) The external electric field E_{ext} dependence of the energy differences $\Delta_{\Gamma-\Gamma}$ and $\Delta_{K-\Gamma}$ for non-polar $\mathrm{MoS_2}$ (olive), $\mathrm{WS_2}$ (blue), and $\mathrm{MoSe_2}$ (red).

is shown as an inset of Fig. 2a. To study the evolution of the band structure on field E_{ext}, we define two quantities, $\Delta_{K-\Gamma} = E_K^{\text{VB}} - E_\Gamma^{\text{VB}}$ and $\Delta_{\Gamma-\Gamma} = E_\Gamma^{\text{CBM}} - E_\Gamma^{\text{VBM}}$, which denote the energy difference between the valence band maximum (VBM) at the K point and the topmost valence band around the Γ point, and the energy difference between the conduction band minimum (CBM) and the VBM at the Γ point, respectively. In the absence of the electric field, the MoS_2 monolayer is a direct gap semiconductor with a positive $\Delta_{K-\Gamma}$ and a large $\Delta_{\Gamma-\Gamma}$ as expected. Because of the absence of the vertical potential gradient, the MoS_2 monolayer has no Rashba splitting as schematically shown in Fig. 1d.

When the electric field increases to 0.5 V Å^{-1}, it becomes an indirect semiconductor with a negative $\Delta_{K-\Gamma}$ and a small $\Delta_{\Gamma-\Gamma}$. A Rashba like spin splitting occurs at the Γ point with a Rashba coefficient of 0.2 eV Å, obtained by using $\alpha_R^{\text{iso}} = \frac{2\Delta E}{\Delta k}$ (schematically shown in Fig. 1e). A larger electric field of 0.75 V Å^{-1} leads to a very large Rashba coefficient of 0.52 eV Å (Fig. 2c and 1f). The behavior of $MoSe_2$ is similar to MoS_2; strikingly, $MoSe_2$ can yield an exceedingly large Rashba coefficient of 1.2 eV Å in the same gate field of 0.75 V Å^{-1}. This value is much larger than that of typical semiconductors [InGaAs/GaAs quantum dots[34] ($\alpha_R \sim 0.08$–0.12 eV Å) or InGaAs/InAlAs heterostructures[17] ($\alpha_R = 0.07$ eV Å)], and heavy metal films commonly studied including the Au(111) surface[13] ($\alpha_R = 0.33$ eV Å) and Au/W(110) quantum wells[35] ($\alpha_R = 0.16$ eV Å), and is slightly larger than the value of 1.1 eV Å for the MoS_2/Bi(111) heterostructure attributed to Bi–Mo orbital hybridization.[36] Understandably, it is smaller than bulk BiTeI[37] ($\alpha_R = 3.8$ eV Å), the Bi/Ag(111) surface[16] ($\alpha_R = 3.05$ eV Å), the single bilayer Bi grown on a single quintuple layer Bi_2Se_3 or Bi_2Te_3 [38] ($\alpha_R \sim 4$ eV Å) and the Pt–Si nanowire[39] ($\alpha_R = 1.36$ eV Å), where the dominant heavy elements introduce a large SOC coupling strength. This is surprising, especially when we consider that both Mo and Se are rather light elements. Moreover, the external gate field provides a controllable way to tune the Rashba spin splitting very effectively.

The gate field applied on the MoS_2 monolayer can in principle change the gradient of the electrostatic potential $V(z)$. To be illustrative, we have calculated the z dependence of the planar averaged electrostatic potential defined as $V(z) = \frac{1}{S}\int V(\vec{r})\mathrm{d}x\mathrm{d}y$, where S is the surface area. The plot is shown in Fig. 2d, where the potential $V(z)$ is shifted with respect to the vacuum level. With the increasing gate field the equivalent valley of the electrostatic potential $V(z)$ around the sulfur plane at the zero electric field (olive line) becomes nonequivalent (blue and red lines), while the change in dipole moments is negligible (Fig. S2b†). Because the screening effect is significantly reduced in the MoS_2 monolayer, a large effective field is presented within the inside region of the monolayer. In contrast, the electrostatic potential $V(z)$ of MoSSe remains unchanged, because the intrinsic dipole moments have a linear dependence on the electric field, which cancels the change in electrostatic potential (Fig. S2a and b†).

According to Poisson's equation, the potential gradient $V(z)$ in MoS_2 created by the electric field results in charge redistribution ($\Delta\rho = \rho_{E_{\text{ext}}=0.5} - \rho_{E_{\text{ext}}=0.0}$), where $\rho_{E_{\text{ext}}=0.5}$ and $\rho_{E_{\text{ext}}=0.0}$ represent the charge density with ($E_{\text{ext}} = 0.0$ V Å^{-1}) and without the gate field ($E_{\text{ext}} = 0.0$ V Å^{-1}), respectively. It can be clearly seen from the inset of Fig. 2d that the p_z orbital of sulfur atoms in MoS_2 is significantly polarized under the electric field. Thanks to the semiconducting nature of monolayer MoS_2, the screening effect can be neglected. Thus the MoS_2 monolayer can be taken as a parallel capacitor approaching the two-dimensional limitation satisfying $\Delta_{\Gamma-\Gamma} = eE_{\text{ext}}\cdot\Delta_{\text{d}}$, where Δ_{d} stands for the distance between the vertically separated sulfur atoms, which corresponds to the slope of each line in Fig. 2e. This linear dependence and the polarized p_z orbital under the electric field are reminiscent of the Stark effect, which represents the energy level splitting in the presence of the strong external gate field. In the present case, the p_z orbital of the sulfur atom on the opposite surfaces of MoS_2 is polarized by the gate field E_{ext}, resulting in a large potential gradient $V(z)$ and subsequently leading to a larger Rashba effect.

The Rashba effect in MoSSe and MoS_2 under an external gate field signifies distinct origins of the intrinsic dipole moment and the induced electrostatic potential gradient, respectively. To generalize this conclusion, we have studied the Rashba effect of other non-polar systems in the same family of TMDs such as WS_2 (blue) and $MoSe_2$ (red), also shown in Fig. 2e and f. The linear dependence of $\Delta_{\Gamma-\Gamma}$ for non-polar WS_2 (blue) and $MoSe_2$ (red) with respect to the gate field remains true, indicating the important role of the Stark effect (Fig. 2e). Moreover, it can be clearly seen that the external field shifts the direct band gap from the K point to the Γ point at a critical field of 0.4–0.6 V Å^{-1} (Fig. 2f).

3.2 Rashba spin splitting and the spin texture

The enlarged view of the valence bands in the MoS_2 monolayer shows an energy splitting in the band maximum along the Γ–K and Γ–M direction, $\Delta_{K-M} = 5.6$ meV (Fig. 3a, and schematically shown in Fig. 1f) in addition to the Rashba momentum splitting. For comparison, we also show the energy splitting of $MoSe_2$ with the external electric field $E_{\text{ext}} = 0.70$ V Å^{-1} along the Γ–K and Γ–M direction (Fig. S4a†). In Fig. 3a the dot size

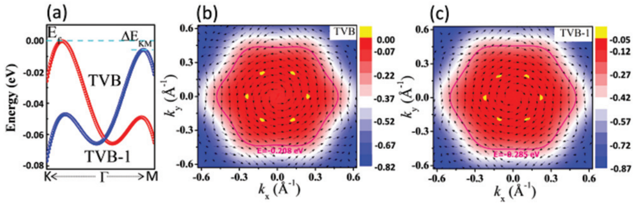

Fig. 3 (a) The enlarged view of TVB in Fig. 2c around the Γ point. The dot size along the Γ–K and Γ–M direction denotes the expected value of the spin operator $\langle S_\alpha(\vec{k})\rangle(\alpha = x, y)$. The red and blue colour represents the spin up and down band, respectively. The VBM is set to zero. (b), (c) The energy contour and spin texture of the top valence band TVB and the neighbouring band below TVB-1 around the Γ point.

along the Γ–K and Γ–M direction denotes the expectation value of the spin operator $\langle S_\alpha(\vec{k})\rangle = \langle\psi(\vec{k})|\sigma_\alpha|\psi(\vec{k})\rangle, (\alpha = x, y)$.[40,41] The red and blue colors represent the spin up and down component, respectively. We also compare the RSS of monolayer MoSe$_2$ and MoS$_2$ in E_{ext} = 0.25 V Å^{-1} (Fig. S3†), which can be easily reached in experiment. To validate the Rashba effect here, we also draw the energy contour and spin texture of the top valence band (TVB) and its neighboring band (TVB-1) around the Γ point in Fig. 3b and c. The pink contour line corresponds to the isosurface of the constant energy value of E = −0.208 eV and −0.285 eV for TVB and TVB-1, respectively. The orientation and magnitude of the arrows in the superimposed spin texture are determined by the spin operator $\langle S_\alpha(\vec{k})\rangle$ along the Γ–K and Γ–M direction. The spin textures of TVB and TVB-1 are anticlockwise and clockwise, respectively. The spin texture of these bands exhibits the overall isotropic Rashba effect in the close vicinity of the Γ point. When the momentum increases further away from the Γ point, the warped band dispersion of MoS$_2$ under E_{ext} = 0.75 V Å^{-1} becomes prominent, as marked by the pink contour line. The yellow color represents the anisotropy between the Γ–K and Γ–M direction. A similar phenomenon existed in the material of MoSe$_2$ (Fig. S4b and c†). Moreover, the anisotropy increases with the increasing wave vector k. The simultaneous occurrence of isotropic, warping and anisotropic band dispersion in the MoS$_2$ monolayer under the gate field strongly suggests that the effective Rashba effect therein could not be simply unified by the previously assumed linear Rashba effect in the level of the free electron model. As a consequence, a nonlinear Rashba effect is required.

3.3 The Rashba parameter dependence on the electric field

The direct consequence of the above nonlinear Rashba effect in MX$_2$ is the nonlinear dependence of the isotropic Rashba coefficient $\alpha_{\text{R}}^{\text{iso}}$ on the external gate field as shown in Fig. 4a (see Fig. S6† for the zoom in plot). For comparison, the isotropic Rashba parameter of the polar-system MoSSe shows a weak and linear dependence on the electric field as expected in conventional narrow-gap semiconductors (Fig. S5 and S6†). These phenomena are consistent with the anisotropic Rashba splitting in the k-space for surface states at Au(110),[42] the Bi/Ag(111) surface alloy,[43] the two-dimensional electron gas in topological insulator heterostructures,[23,44,45] *etc.*

The nonlinear dependence of the Rashba effect on the external gate field can be explained by the ***k·p*** model *via* the following symmetry analysis. Monolayer MX$_2$ is invariant under the $D_{3\text{h}}$ symmetry, which consists of two operations: a trigonal $C_{3\text{v}}$ rotation and a mirror reflection M ($z \to -z$) with respect to the hexagonal plane. For a two-dimensional system with $C_{3\text{v}}$ symmetry, a two-band effective Hamiltonian $H_{\text{R}}(k)$ for the Rashba effect up to cubic terms of momentum k reads[43,46–49]

$$H_{\text{R}}(k) = (\alpha_1 k + {\alpha_3}^1 k^3)(\cos\varphi\sigma_y - \sin\varphi\sigma_x) + {\alpha_3}^2 k^3 \cos 3\varphi\sigma_z \tag{1}$$

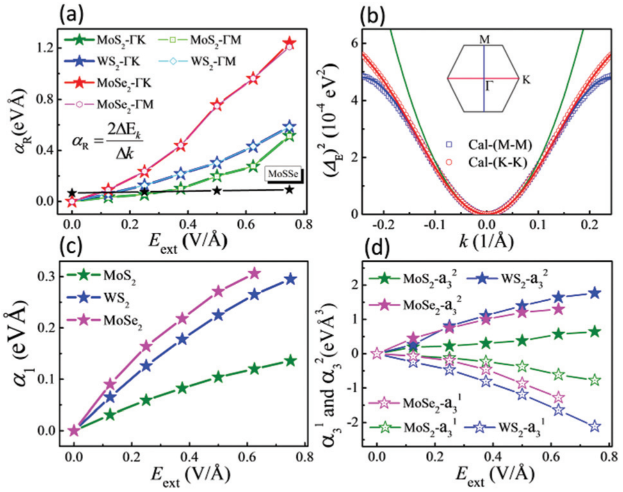

Fig. 4 (a) The linear Rashba parameters calculated by using $\alpha_{\text{R}} = \dfrac{2\Delta E}{\Delta k}$ along the Γ–K (filled symbols) and Γ–M (empty symbols) direction. (b) The squared energy splitting $\Delta E(k)^2$ for the occupied states of MoS$_2$ with E_{ext} = 0.75 V Å^{-1} along the Γ–K (red circle) and Γ–M (blue square) direction. (c), (d) The external electric field E_{ext} dependence of the first order α_1, third-order isotropic ${a_3}^1$ and anisotropic ${a_3}^2$ parameters for MoS$_2$ (olive), WS$_2$ (blue) and MoSe$_2$ (magenta) respectively.

with the polar coordinate φ = acrcos(k_x/k). Note that the k_x axis was chosen to be along the Γ–K direction of the first Brillouin zone. Here,

$${\alpha_3}^1 = \frac{\hbar^4}{4m^4c^2}\sum_{n,m}\frac{\langle\varphi_0|p_x|{\varphi_n}^+\rangle\langle{\varphi_n}^+|\partial_z V|{\varphi_m}^+\rangle\langle{\varphi_m}^+|p_x|\varphi_0\rangle}{(\varepsilon_0 - \varepsilon_n^E)(\varepsilon_0 - \varepsilon_m^E)}$$

$${\alpha_3}^2 = \frac{\hbar^4}{4m^4c^2}\sum_{n,m}\frac{\langle\varphi_0|p_x|{\varphi_n}^+\rangle\langle{\varphi_n}^+|\partial_x V|{\varphi_m}^+\rangle\langle{\varphi_m}^+|p_x|\varphi_0\rangle}{(\varepsilon_0 - \varepsilon_n^E)(\varepsilon_0 - \varepsilon_m^E)}$$

From the above formulae, we see that ${\alpha_3}^1$ depends on the partial derivative of the crystal potential normal to the surface $\partial_z V$, while the coefficient for the anisotropic term ${\alpha_3}^2$ is related to the in-plane gradient of the potential $\partial_x V$. Besides the first-order linear term α_1, there are obviously two third-order terms contributing to the Hamiltonian: an isotropic one with the coefficient ${\alpha_3}^1$ and an anisotropic one from the warping effect with the coefficient ${\alpha_3}^2$.[50] The squared energy splitting can be expressed as:

$$\Delta E(k)^2 = (\alpha_1 k + {\alpha_3}^1 k^3)^2 + ({\alpha_3}^2)^2 k^6 \cos^2 3\varphi, \tag{2}$$

where the energy splitting of the two branches of RSS is $\Delta E(k)$ = $[\varepsilon_+(k) - \varepsilon_-(k)]/2$.

Fig. 4b shows the $\Delta E(k)^2$ of the occupied Rashba states under the electric field of 0.75 V Å^{-1} along the Γ–M (blue squares) and Γ–K directions (red circles). A parabolic fit ${\alpha_1}^2 k^2$ (olive line) to the calculated $\Delta E(k)^2$ as the main contribution can coincide up to $k \approx \pm 0.08$ Å^{-1} with a linear Rashba parameter of α_1 = 0.136 eV Å. At a larger momentum (k > 0.13 Å^{-1}), the warping effect of the Rashba splitting becomes apparent, indicating that the third-order contribution is needed for a good fit. Here if we use only α_1 = 0.136 eV Å and

$\alpha_3{}^1 = -0.776$ eV Å^3, we obtain a good fit along Γ–M ($\varphi = \pi/2$) (blue square in Fig. 4b), but fail along the Γ–K ($\varphi = 0$) direction. To fix this problem the anisotropic term of eqn (2) has to be included, where we find that $\alpha_3{}^2 = 0.642$ eV Å^3. The fitted curves are in excellent agreement with the first-principles data (Fig. 4b).

The dependence of parameters α_1, $\alpha_3{}^1$, and $\alpha_3{}^2$ on the electric field is plotted in Fig. 4c and d. We find that the slope of α_1 in $MoSe_2$ (magenta) is larger than that of WS_2 (blue) when taking the slope of MoS_2 (olive) as a reference. The expected linear dependence of α_1 in MX_2 on the electric field shown in Fig. 4c indicates that the polarization of the non-metal atom X plays a more significant role than the atomic spin orbit coupling of M atoms, because of the large atomic orbital radius of non-metal atoms. The third-order terms $\alpha_3{}^1$, $\alpha_3{}^2$ are responsible for the anisotropy and warping effect of the Rashba splitting. Fig. 4d shows the electric field dependence of the $\alpha_3{}^1$ and $\alpha_3{}^2$ for MoS_2 (olive), WS_2 (blue) and $MoSe_2$ (magenta), respectively. It can be clearly seen that the negative $\alpha_3{}^1$ and positive $\alpha_3{}^2$ are linearly dependent on the gate field. Moreover, the absolute slope of $\alpha_3{}^1$ and $\alpha_3{}^2$ for WS_2 is larger than for $MoSe_2$ indicating that the spin–orbit coupling of metal atoms plays a dominant role over the polarization of non-metal atomic orbitals in the high-order terms.

3.4 The spintronics device schematic and anisotropic energy splitting of the top valence bands

The anisotropic energy splitting Δ_{K-M} of the top valence band along the Γ–M and Γ–K direction can be tuned *via* an external gate field, where the broken degeneracy of the VBM around the Γ point leads to the broken degeneracy of spin-up $|\uparrow\rangle$ and spin-down $|\downarrow\rangle$ electrons. If the monolayer TMD is doped by electron acceptors, the Fermi level will cross one of the spin channels generating spin-polarized electrons (or spin currents). Consequently the p-doped monolayer TMDs under the gate field can act as spin injection devices (Fig. 5a). Moreover, the anisotropic energy splitting Δ_{K-M} can be tuned by the external gate field, which can be achieved by a strong dipole interface ($PbTiO_3$, *etc.*), promoted by the gating voltage and ionic liquids,[51–53] or probing the monolayer TMD materials under the scanning tunnelling microscopy (STM) tip locally. At the present experimental level, the value of the electric field at the ionic liquid/Au interface is estimated to be as large as 0.27 eV Å^{-1},[54] which could provide a potential way to justify the theoretical predictions discussed above. In Fig. 5b, olive, blue and red stars denote the anisotropic energy splitting Δ_{K-M} for MoS_2, WS_2, and $MoSe_2$, respectively. We see that the anisotropic energy splitting Δ_{K-M} increases with the increasing gate field. The anisotropic coefficient $\alpha_3{}^2$ responsible for this energy splitting Δ_{K-M} can enable single spin polarization if the Fermi level is located at the interval of the top-two valence bands (Fig. 3a and the inset of Fig. 5b). In particular, the anisotropic energy splitting of $MoSe_2$ can reach as large as 25 meV, larger than that in bulk BiTeI and BiTeI/Bi_2Te_3 heterostructures of about 15 meV (ref. 23) and the monolayer WSe_2 of about 15.7 meV (Fig. S7†), which would allow the *p*-type itinerant magnetism at room temperature.[55]

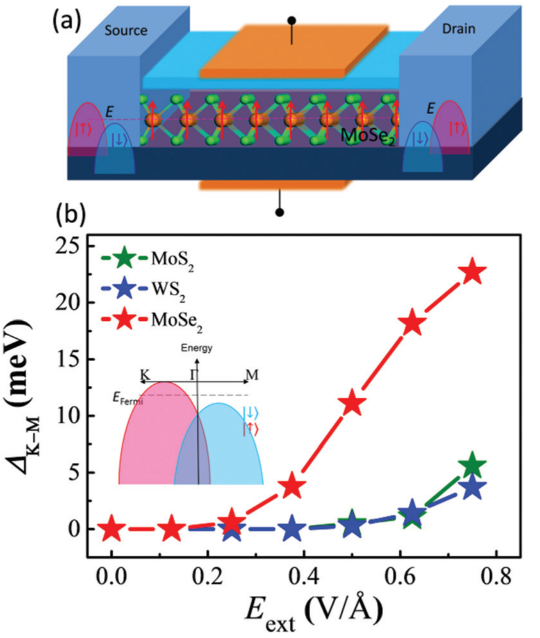

Fig. 5 (a) Schematic view of the spin filter by applying the gate voltage to the monolayer $MoSe_2$. (b) The electric field dependence of the energy splitting Δ_{K-M} of the TVB (see Fig. 3a) for MoS_2 (olive), WS_2 (blue) and $MoSe_2$ (red). The inset is the same as Fig. 1f.

4. Conclusions

To summarize, a large nonlinear Rashba effect is predicted by first-principles to emerge in the single layer MX_2 under a perpendicular electric field. The anisotropy of RSS is found to be qualitatively different from the conventional linear relationship with the increasing external electric field. Based on a $\boldsymbol{k}\cdot\boldsymbol{p}$ model *via* symmetry analysis, the higher order terms are found to be responsible for the nonlinear Rashba splitting. As a result, the largest anisotropy in RSS is achieved in $MoSe_2$ under a large gate field. The giant anisotropic energy splitting Δ_{K-M} might enable spin injection or filter devices in spintronics applications. The effect presented here could trigger further experiments where a large electric field might be realized *via* ionic-liquid gating or polar ferroelectric gate methods.

Acknowledgements

This work acknowledge financial support from the National Basic Research Program of China (Grant No. 2016YFA0300902, 2013CBA01600, and 2015CB921001), the National Natural Foundation of China (Grant No. 61306114 and 11222431), the "Strategic Priority Research Program (B)" of the Chinese Academy of Sciences (Grant No. XDB07030100), and the NSAF (Grant No. U1430117). We also acknowledge the computing resources from the Tianjin Supercomputing Center.

References

1 K. S. Novoselov, D. Jiang, F. Schedin, T. J. Booth, V. V. Khotkevich, S. V. Morozov and A. K. Geim, *Proc. Natl. Acad. Sci. U. S. A.*, 2005, **102**, 10451–10453.

2 B. Radisavljevic, A. Radenovic, J. Brivio, V. Giacometti and A. Kis, *Nat. Nanotechnol.*, 2011, **6**, 147–150.

3 K. F. Mak, C. Lee, J. Hone, J. Shan and T. F. Heinz, *Phys. Rev. Lett.*, 2010, **105**, 136805.

4 D. Xiao, G. B. Liu, W. Feng, X. Xu and W. Yao, *Phys. Rev. Lett.*, 2012, **108**, 196802.

5 H. Zeng, J. Dai, W. Yao, D. Xiao and X. Cui, *Nat. Nanotechnol.*, 2012, **7**, 490–493.

6 K. F. Mak, K. He, J. Shan and T. F. Heinz, *Nat. Nanotechnol.*, 2012, **7**, 494–498.

7 T. Cao, G. Wang, W. Han, H. Ye, C. Zhu, J. Shi, Q. Niu, P. Tan, E. Wang, B. Liu and J. Feng, *Nat. Commun.*, 2012, **3**, 887.

8 Z. Yin, H. Li, H. Li, L. Jiang, Y. Shi, Y. Sun, G. Lu, Q. Zhang, X. Chen and H. Zhang, *ACS Nano*, 2012, **6**, 74–80.

9 X. Qian, J. Liu, L. Fu and J. Li, *Science*, 2014, **346**, 1344–1347.

10 E. I. Rashba, *Sov. Phys. Solid State*, 1960, **2**, 1109.

11 Y. A. Bychkov and E. I. Rashba, *JETP Lett.*, 1984, **39**, 78–81.

12 Y. A. Bychkov and E. I. Rashba, *J. Phys. C: Solid State Phys.*, 1984, **17**, 6039–6045.

13 S. LaShell, B. A. McDougall and E. Jensen, *Phys. Rev. Lett.*, 1996, **77**, 3419.

14 Y. M. Koroteev, G. Bihlmayer, J. E. Gayone, E. V. Chulkov, S. Blugel, P. M. Echenique and P. Hofmann, *Phys. Rev. Lett.*, 2004, **93**, 046403.

15 M. Hoesch, M. Muntwiler, V. N. Petrov, M. Hengsberger, L. Patthey, M. Shi, M. Falub, T. Greber and J. Osterwalder, *Phys. Rev. B: Condens. Matter*, 2004, **69**, 241401(R).

16 C. R. Ast, J. Henk, A. Ernst, L. Moreschini, M. C. Falub, D. Pacile, P. Bruno, K. Kern and M. Grioni, *Phys. Rev. Lett.*, 2007, **98**, 186807.

17 J. Nitta, T. Akazaki and H. Takayanagi, *Phys. Rev. Lett.*, 1997, **78**, 1335.

18 M. Schultz, F. Heinrichs, U. Merkt, T. Collin, T. Skauli and S. Løvold, *Sci. Technol.*, 1996, **1111**, 68–72.

19 K. He, T. Hirahara, T. Okuda, S. Hasegawa, A. Kakizaki and I. Matsuda, *Phys. Rev. Lett.*, 2008, **101**, 107604.

20 E. Frantzeskakis, S. Pons, H. Mirhosseini, J. Henk, C. R. Ast and M. Grioni, *Phys. Rev. Lett.*, 2008, **101**, 196805.

21 P. D. C. King, R. C. Hatch, M. Bianchi, R. Ovsyannikov, C. Lupulescu, G. Landolt, B. Slomski, J. H. Dil, D. Guan, J. L. Mi, E. D. Rienks, J. Fink, A. Lindblad, S. Svensson, S. Bao, G. Balakrishnan, B. B. Iversen, J. Osterwalder, W. Eberhardt, F. Baumberger and P. Hofmann, *Phys. Rev. Lett.*, 2011, **107**, 096802.

22 Z. H. Zhu, G. Levy, B. Ludbrook, C. N. Veenstra, J. A. Rosen, R. Comin, D. Wong, P. Dosanjh, A. Ubaldini, P. Syers, N. P. Butch, J. Paglione, I. S. Elfimov and A. Damascelli, *Phys. Rev. Lett.*, 2011, **107**, 186405.

23 J. J. Zhou, W. Feng, Y. Zhang, S. A. Yang and Y. Yao, *Sci. Rep.*, 2014, **4**, 3841.

24 H. Min, J. E. Hill, N. A. Sinitsyn, B. R. Sahu, L. Kleinman and A. H. MacDonald, *Phys. Rev. B: Condens. Matter*, 2006, **74**, 165310.

25 G. Kresse and J. Hafner, *Phys. Rev. B: Condens. Matter*, 1993, **47**, 558.

26 G. Kresse and J. Hafner, *Phys. Rev. B: Condens. Matter*, 1994, **49**, 14251.

27 G. Kresse and J. Furthmüller, *Phys. Rev. B: Condens. Matter*, 1996, **54**, 11169.

28 P. E. Blochl, *Phys. Rev. B: Condens. Matter*, 1994, **50**, 17953.

29 J. P. Perdew, K. Burke and M. Ernzerhof, *Phys. Rev. Lett.*, 1996, **77**, 3865.

30 H. J. Monkhorst and J. D. Pack, *Phys. Rev. B: Condens. Matter*, 1976, **13**, 5188.

31 J. Neugebauer and M. Scheffler, *Phys. Rev. B: Condens. Matter*, 1992, **46**, 16067.

32 X. Gonze and C. Lee, *Phys. Rev. B: Condens. Matter*, 1997, **55**, 10355.

33 S. Baroni, S. D. Gironcoli and A. D. Corso, *Rev. Mod. Phys.*, 2001, **73**, 515.

34 S. M. Huang, A. O. Badrutdinov, L. Serra, T. Kodera, T. Nakaoka, N. Kumagai, Y. Arakawa, D. A. Tayurskii, K. Kono and K. Ono, *Phys. Rev. B: Condens. Matter*, 2011, **84**, 085325.

35 A. Varykhalov, J. Sanchez-Barriga, A. M. Shikin, W. Gudat, W. Eberhardt and O. Rader, *Phys. Rev. Lett.*, 2008, **101**, 256601.

36 K. Lee, W. S. Yun and J. D. Lee, *Phys. Rev. B: Condens. Matter*, 2015, **91**, 125420.

37 K. Ishizaka, M. S. Bahramy, H. Murakawa, M. Sakano, T. Shimojima, T. Sonobe, K. Koizumi, S. Shin, H. Miyahara, A. Kimura, K. Miyamoto, T. Okuda, H. Namatame, M. Taniguchi, R. Arita, N. Nagaosa, K. Kobayashi, Y. Murakami, R. Kumai, Y. Kaneko, Y. Onose and Y. Tokura, *Nat. Mater.*, 2011, **10**, 521–526.

38 Z. F. Wang, M. Y. Yao, W. Ming, L. Miao, F. Zhu, C. Liu, C. L. Gao, D. Qian, J. F. Jia and F. Liu, *Nat. Commun.*, 2013, **4**, 1384.

39 J. Park, S. W. Jung, M. C. Jung, H. Yamane, N. Kosugi and H. W. Yeom, *Phys. Rev. Lett.*, 2013, **110**, 036801.

40 O. V. Yazyev, J. E. Moore and S. G. Louie, *Phys. Rev. Lett.*, 2010, **105**, 266806.

41 W. Ming, Z. F. Wang, M. Zhou, M. Yoon and F. Liu, *Nano Lett.*, 2016, **16**, 404–409.

42 M. Nagano, A. Kodama, T. Shishidou and T. Oguchi, *J. Phys.: Condens. Matter*, 2009, **21**, 064239.

43 S. Vajna, E. Simon, A. Szilva, K. Palotas, B. Ujfalussy and L. Szunyogh, *Phys. Rev. B: Condens. Matter*, 2012, **85**, 075404.

44 E. Frantzeskakis and M. Grioni, *Phys. Rev. B: Condens. Matter*, 2011, **84**, 155453.

45 M. Michiardi, M. Bianchi, M. Dendzik, J. A. Miwa, M. Hoesch, T. K. Kim, P. Matzen, J. Mi, M. Bremholm, B. B. Iversen and P. Hofmann, *Phys. Rev. B: Condens. Matter*, 2015, **91**, 035445.

46 T. Oguchi and T. Shishidou, *J. Phys.: Condens. Matter*, 2009, **21**, 092001.

47 E. Simon, A. Szilva, B. Ujfalussy, B. Lazarovits, G. Zarand and L. Szunyogh, *Phys. Rev. B: Condens. Matter*, 2010, **81**, 235438.

48 M. S. Bahramy, B. J. Yang, R. Arita and N. Nagaosa, *Nat. Commun.*, 2012, **3**, 679.

49 H. Yuan, M. S. Bahramy, K. Morimoto, S. Wu, K. Nomura, B.-J. Yang, H. Shimotani, R. Suzuki, M. Toh, C. Kloc, X. Xu, R. Arita, N. Nagaosa and Y. Iwasa, *Nat. Phys.*, 2013, **9**, 563–569.

50 L. Fu, *Phys. Rev. Lett.*, 2009, **103**, 266801.

51 F. Wang, P. Stepanov, M. Gray, C. N. Lau, M. E. Itkis and R. C. Haddon, *Nano Lett.*, 2015, **15**, 5284–5288.

52 H. Mirhosseini, I. V. Maznichenko, S. Abdelouahed, S. Ostanin, A. Ernst, I. Mertig and J. Henk, *Phys. Rev. B: Condens. Matter*, 2010, **81**, 073406.

53 A. Nguyen, P. Sharma, T. Scott, E. Preciado, V. Klee, D. Sun, I. H. Lu, D. Barroso, S. Kim, V. Y. Shur, A. R. Akhmatkhanov, A. Gruverman, L. Bartels and P. A. Dowben, *Nano Lett.*, 2015, **15**, 3364–3369.

54 H. Nakayama, J. Ye, T. Ohtani, Y. Fujikawa, K. Ando, Y. Iwasa and E. Saitoh, *Appl. Phys. Express*, 2012, **5**, 023002.

55 T. Cao, Z. Li and S. G. Louie, *Phys. Rev. Lett.*, 2015, **114**, 236602.